

## Influence of scale effect on flow field offset for ships in confined waters

ZhongXin Ma, Nan Ji\*, Qian Zeng, XiaoBing Deng, Cong Shi

School of Shipping and Naval Architecture, Chongqing Jiao Tong University, Chongqing 400074, China

### ARTICLE INFO

Editor-in-Chief: Prof. Nastia Degiuli

Associate Editor: PhD Ivana Martić

Scale effect

Shallow water

Ship-bank interaction

Migration of flow field

Body force method

Virtual disk

### ABSTRACT

To investigate the flow field characteristics of full-scale ships advancing through confined waters, the international standard container ship (KRISO Container Ship) was considered as a research object in this study. Using the RANS equation, the volume of fluid method and the body force method were selected to investigate the hydrodynamic characteristics of a model-scale ship (the model-scale ratio  $\lambda=31.6$ ) and a full-scale ship advancing through confined waters at low speed. A virtual disk was used in the full-scale model to determine the influence of the propeller on the ship's flow field. First, the feasibility of the numerical calculations was verified. This proves the feasibility of the numerical and grid division methods. The self-propulsion point of the full-scale ship at  $Fr=0.108$  is determined. The calculation cases of model-scale and full-scale ships (with or without virtual disks) at different water depths and distances between the ship and the shore were calculated, and the changes in the hull surface pressure, the flow field around the ship, and the wake fraction near the ship propeller disk in different calculation cases were determined and compared. The variations in the surge force, sway force, and yaw moment between the model-scale and full-scale ships were generally consistent. In very shallow water ( $H/T=1.3$ ), the non-dimensional force and moment coefficients for model-scale ships increase more rapidly with decreasing distance from shore, suggesting that using model-scale ships to investigate the wall effect in very shallow water will result in predictions that are biased towards safety. By comparing full-scale ships with and without propellers, it was discovered that the surge force, sway force, and yaw moment were marginally greater in the propeller-equipped ship due to the suction effect, and the accompanying flow before and after the propeller was slightly smaller, with less asymmetry.

### Introduction

Driven by economic development, the size of ships continues to increase, making the dredging and restoration of waterways and harbours an ever-greater challenge. Compared with unrestricted service areas, the hydrodynamic characteristics and navigational condition of ships are adversely affected by confined waters. The grounding accident at the Suez Canal in 2021 served as a wake-up call for ship operators. When ships navigate in confined waters such as canals and ports, they are extremely vulnerable to shallow water and

\* Corresponding author.

E-mail address: [jinan@cqjtu.edu.cn](mailto:jinan@cqjtu.edu.cn)

bank effects. This, in turn, alters the forces acting on the ship and the flow field around the ship [1,2], which ultimately leads to safety incidents.

Variations in ship scale make it infeasible to maintain consistent Reynolds numbers in theoretical computations, leading to discrepancies between the flow fields of model- and full-scale ships [3]. A few discrepancies have been observed between the experimental results of the ship models at different scales. For example, Shivachev et al. [4] measured a trim of  $0.162^\circ$  at a scale factor of  $\lambda=75$  and Simonsen et al. [5] reported a trim of  $0.185^\circ$  for  $\lambda=52.667$  at the same Froude number. Although the numerical values differ slightly, we cannot dismiss the influence of the scale effects. It has been proven that sinkage and trim vary with scale factor both numerically [5-7] and experimentally [8]. However, in recent related research, numerical studies on the scale effect of ship squat predicted a deviation between dimensionless sinkage of approximately 5% [9]. Therefore, it is reasonable to neglect sinkage and trim to isolate their effects on the resistance [10].

It is known that larger scale effects occur in shallow and confined water areas, primarily owing to the interaction of the ship with the seabed. As previously noted, the near-field disturbance was influenced to a greater extent by scale effects. This, and the fact that the seabed can potentially form a boundary layer, explains why a magnified scale effect is to be expected [11]. Consequently, at various scales, the flow properties in the gap between hull and seabed or canal sides vary in line with the Reynolds numbers, and not the linear scales.

Computational fluid dynamics (CFD) has been extensively used in the analysis of ship hydrodynamic performance. Owing to the proliferation of computer technology, full-scale ship research is becoming increasingly popular [12-14]. The selection of parameters, such as the turbulence model and boundary layer, has a certain influence on the numerical simulation of full-scale ships, and the value of  $Y^+$  for full-scale ships will also be correspondingly larger [15-18]. Mikkelsen and Walther [19] noted that the direct application of a roughness model into the CFD simulation yields a more precise result than the conventional approach that relies on empirical formulas specifically designed for towing tanks. Zhang et al. [20] simulated the influence of a slipstream on the sway load of a propeller at three scales and showed that the change of scale had little effect on the horizontal load of the propeller, However the scale effect caused a relatively large change in the longitudinal flow velocity. Dogrul [21] studied the scale effects on the propulsive parameters of a Joubert BB2 submarine with a MARIN7371R propeller using the body force method to minimise the consumption of computational resources. Đurasević et al. [22] proposed a rotating grid method applicable for ship self-propulsion and analysed the flow characteristics in terms of ship-propeller interaction and scale effects. They explained that different boundary-layer thicknesses and Reynolds numbers at different scales can affect the performance and simulation of propellers. Terziev et al. [10] pointed out that the wake variations for full-scale ships navigating through confined waters are more gradual than in model-scale numerical simulations by examining the flow velocity and boundary layer thickness. Liu et al. [23] used regression analysis and a Fourier integral, substituted asymmetric hydrodynamic derivatives into the equations of manoeuvring motion to identify the hydrodynamic derivatives, and calculated the rudder angles and heading angles at different water depths. The increasing asymmetric hydrodynamic forces can dramatically affect some parameters of the course-keeping criteria as the distance between the ship and the shore decreases.

Hoydonck et al. [24] investigated the interactions between a ship and bank using two different CFD codes, using viscous flow solution methods to forecast the hydrodynamic forces and moments acting on a ship close to the bank. Hadi et al. [25] evaluated the hydrodynamic interaction of the 750 DWT Perintis Ship moving through different canal types and proposed that ships with higher speeds were more sensitive to changes in waterway restrictions. Yuan [26] improved a new method of calculating the potential flow to address ship-to-ship issues within confined waterways and preferably achieved expectations. Elsherbiny et al. [27] simulated the passage of a KCS through the Suez Canal and examined the impacts of different channel shapes on the squat and trim of a ship. Raven [28] studied the influence of water depth on the resistance of ships and adopted a new correction method to better predict the resistance of full-scale ships. Ulgen and Dhanak [29] used the incompressible URANS-VOF solver in OpenFOAM to investigate the influence of finite water depth on the hydrodynamic performance of catamarans, and discussed the relationships between ship waves, drag, trim, and sinking. Lee [30] investigated the influence of various factors, such as the water depth-to-draft ratio and speed, on the hydrodynamic performance of ships by changing the calculation cases. Poojari

and Kar [31] found that the conclusions from scale effect studies indicate that wake flow is highly sensitive to scale effects, which necessitates the consideration of full-scale conditions. The axial flow toward the propeller was influenced by the motion of the ship near the wall. A higher degree of reverse flow is observed with increasing proximity of the ship to the wall, and an asymmetric wake at the propeller plane can degrade the performance of the ship and reduce the ability to produce thrust at given rotational speeds. Lo and Lin [32] simulated the bank effect on a KRISO 3600 TEU container ship model using FLOW3D CFD software and proved that the bank effect increased significantly when the ship model velocity exceeded  $V=0.55$  m/s. To minimise the bank effect, ships should travel at lower speeds in restricted waters. Using the CFD method, Zou et al. [33] and Zou [34] examined the bank effect of a tanker moving straight ahead at low speed in a canal characterised by surface-piercing banks. Their research included verification and validation through grid convergence studies and comparison with experimental data, as well as investigation of modelling errors in RANS computations to predict bank effects more accurately and reliably. It is worth mentioning that Zou and Larsson [35] applied CFD to analyse the influence of propulsion force on the bank suction. They concluded that the propeller increases the velocity around the stern of the ship, which is equivalent to an unimpeded flow. However, owing to the extremely low velocity on the starboard side (vertical wall), half of the propeller bears a heavier load. Therefore, more flow is absorbed on the starboard side, and the reduced pressure generate a bow-out moment on the hull.

Currently, overset grids are widely used in the numerical simulation of hull-propeller-rudder systems and their coupled motions. Castro et al. [36] used overset grid techniques to verify the feasibility of a full-scale self-propulsion simulation of a KRISO Container Ship (KCS) and proposed a method to calculate the roughness of the sand grain equivalent. Carrica et al. [37] and Islam and Soares [38] performed the corresponding grid verification and studied the hydrodynamic performance of the KCS ship model in a restricted water channel using overset grids.

The influence of the propeller on the flow field of a ship is of utmost importance. Therefore, it is necessary to numerically investigate the flow field of ships navigating in restricted waters owing to the effects of the scale effect and the propeller.

This paper focuses on the KCS as a research object and conducts numerical calculations for different draft ratios and distances between ship and shore under three models: model-scale ship, full-scale ship without a propeller, and full-scale ship with a virtual disk simulating the role of the propeller. It analysed the computational conditions under different restricted scenarios, including scale effects and propeller additions. This study investigated the effects of shallow water banks, scale effects, and propeller-induced suction on the flow fields and hull forces of ships in restricted water conditions.

## 1. Numerical Methods

### 1.1 Fluid control equations and turbulence modelling

The fluid around the hull is an incompressible flow based on the RANS equation used to solve the Navier-Stokes equations, as expressed in Equations (1) and (2):

$$\frac{\partial u_i}{\partial x_i} = 0 \quad (1)$$

$$\rho \frac{\partial u_i}{\partial t} + \rho u_j \frac{\partial u_i}{\partial x_j} = -\frac{\partial P}{\partial x_i} + \frac{\partial}{\partial x_j} \left( \mu \frac{\partial u_i}{\partial x_j} - \overline{\rho u'_i u'_j} \right) \quad (2)$$

where:  $u_i$  and  $u_j$  are the averaged Cartesian components of the velocity vector;  $\rho$ ,  $P$ ,  $\mu$  are the water density, mean pressure, and kinematic viscosity of water, respectively;  $x_i$  and  $x_j$  are the spatial coordinate components;  $t$  is the time; and  $\overline{\rho u'_i u'_j}$  is the Reynolds stresses.

To account more accurately for the effects of wave generation on the hydrodynamic properties of ships, the volume of fluid (VOF) method was used to capture the interface and treat the water surface. The near-wall treatment with the All  $Y^+$  wall treatment, and the use of SST  $k-\omega$  [39] turbulence modelling are expressed as Equations (3) and (4):

$$\frac{\partial(\rho k)}{\partial t} + \frac{\partial(\rho k u_i)}{\partial x_i} = \frac{\partial}{\partial x_j} \left[ \Gamma_k \frac{\partial k}{\partial x_j} \right] + G_k - Y_k \quad (3)$$

$$\frac{\partial(\rho \omega)}{\partial t} + \frac{\partial(\rho \omega u_i)}{\partial x_i} = \frac{\partial}{\partial x_j} \left[ \Gamma_\omega k \frac{\partial k}{\partial x_j} \right] + G_\omega - Y_\omega + D_\omega \quad (4)$$

where  $k$  is the flux energy,  $\omega$  is the dissipation rate,  $\Gamma$  is the effective diffusivity,  $G$  is the generation term,  $Y$  is the diffusion term, and  $D$  is the cross-diffusion term.

## 1.2 Control of the self-propulsion

The speed of the propeller was regulated by implementing a  $PI$  controller [36], and the target navigation speed was achieved by adjusting the propeller speed, as shown in Equations (5) and (6):

$$e_U = U_{\text{target}} - U_{\text{ship}} \quad (5)$$

$$n = Pe + I \int_0^t e dt \quad (6)$$

where  $e_U$  is the difference between the target speed  $U_{\text{target}}$  and the real-time speed  $U_{\text{ship}}$ ;  $n$ ,  $t$ ,  $dt$  are the rotational speed of the propeller, the rotation time and the unit time step, respectively;  $P$  is the constant of proportionality, and  $I$  is a constant of integration, which was set to  $P=I=40$  in this study.

## 2. Numerical Verification

### 2.1 Computational model

The international standard container ship KCS was the subject of this study with a scale ratio of 1:31.6. The model of the ship body is illustrated in Fig. 1, and the geometric parameters of the ship body and the KP505 propeller are listed in Table 1.

The centroid of the ship is considered the origin of the coordinate system, with the  $x$ -axis pointing towards the bow of the ship, the  $y$ -axis towards the left side of the ship, and the  $z$ -axis upward. The surge force  $X$  points to the rear, the sway force  $Y$  points to the starboard side (i.e. it is positive when pointing towards the vertical wall), the yaw moment  $M_N$  is positive when the port side is pushed into the water, and the yaw moment  $M_N$  is positive when the bow is pushed to the left (i.e. away from the vertical hull).

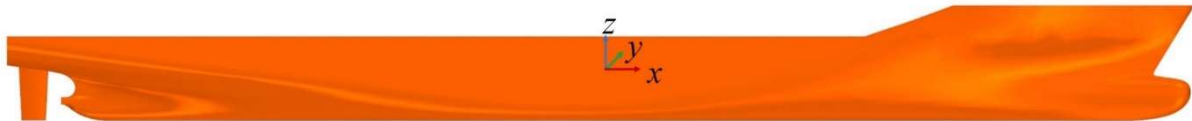


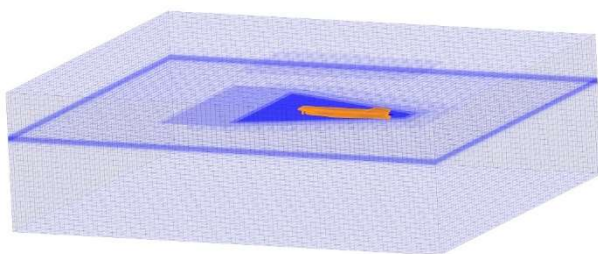
**Fig. 1.** The model of the hull

**Table 1.** KCS geometry

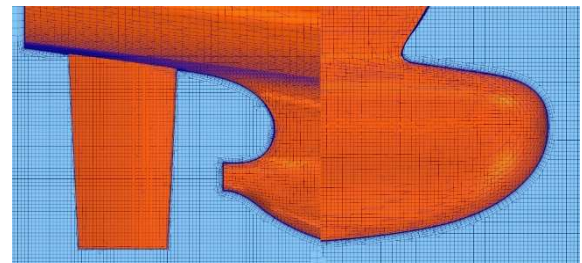
Parameters	Symbol	Full-scale	Model-scale
Scale ratio	$\lambda$	1	31.6
Length between perpendiculars	$L_{PP}$ (m)	230	7.2786
Maximum beam of waterline	$B$ (m)	32.2	1.0190
Draft	$T$ (m)	10.8	0.3418
Displacement volume	$\nabla$ (m <sup>3</sup> )	52030	0.6505
Wetted surface area w/o rudder	$S_W$ (m <sup>2</sup> )	9539	9.5531
Block coefficient	$C_B$	0.6505	0.6505
Longitudinal centre of buoyancy	% $L_{BP}$ , fwd+	-1.48	-1.48
The metacentric height	$G_M$ (m)	0.6	0.019
Radius of gyration	$K_{XX}/B$	0.49	0.49
Radius of gyration	$K_{YY}/L_{BP}$ , $K_{ZZ}/L_{BP}$	0.25	0.25
Propeller Diameter	$D$ (m)	7.9	0.25
Propeller center, long. location (from Aft Perpendicular)	$x/L_{PP}$	0.9825	0.9825
Propeller center, vert. location (below Water Line)	$-z/L_{PP}$	0.02913	0.02913
Propeller rotation direction (view from stern)	-	clockwise	clockwise

## 2.2 Mesh resolution

According to [40], the grid independence and convergence of the computational results of the model were analysed. In the centroid coordinate system, the computational domain grid range is defined as follows:  $-2.5L_{PP} \leq x \leq 1.5L_{PP}$ ,  $-2L_{PP} \leq y \leq 2L_{PP}$ ,  $-1L_{PP} \leq z \leq 0.5L_{PP}$ ; the boundary near the stern of the ship is set as a pressure outlet, with the remaining boundaries set as velocity inlets. The mesh-generation process is shown in Fig. 2.



(a) The computational domain and grid division



(b) Schematic diagram of the head and the tail grid of the ship

**Fig. 2.** Mesh generation around the KCS

The  $Y^+$  value of the model-scale ship was calculated as less than 60 [40]. The full-scale ship should have a rough wall surface and the equivalent sand grain diameter is set according to literature [36]. As the full-scale ship has a higher Reynolds number, the maximum  $Y^+$  value less than 500 is also within the acceptable range

[15,17]. According to Lee et al. [41], the range of  $\Delta t \leq 0.0025 L_{PP}/U$  for the selection of the time step ( $\Delta t$ ), where  $L_{PP}$  and  $U$  represent the ship length and ship speed, respectively. The time step size for the model-scale simulations was set to  $\Delta t = 0.02$  s, the time step size for the full-scale simulations was set to  $\Delta t = 0.05$  s.

$R_G$ ,  $GCI$ ,  $TCI$  represent the convergence ratio, the medium-grid convergence index, and the medium-time convergence index, respectively. This indicates that the calculation results converge monotonically when  $0 < R_G < 1$ . The three grid sets and time steps are generated by applying ratio  $r_G = \sqrt{2}$ .

The calculation results of the ship model were validated by a comparison with the 2015 Tokyo Workshop [42] and the full-scale ship calculation results were validated against values from the literature [36]. The results of the grid calculation convergence are listed in Table 2. A medium grid set was used for the investigated time-step sizes, and the numerical results are listed in Table 3. To ensure the rationality of the subsequent computations, the scenarios of the model-scale ship for  $\eta/B=1.3$  and  $H/T=1.3$  were also considered at  $Fr=0.108$ , as listed in Table 4.

**Table 2.** Grid convergence study

	Grid set	Grid volumes	$C_T$ [42,36]	$C_T$ of CFD	Error (%)	$R_G$	$GCI$ (%)
Model-scale ship ( $Fr=0.108$ )	Coarse	$1.30 \times 10^6$	$3.796 \times 10^{-3}$	$3.998 \times 10^{-3}$	5.32	0.39	2.36
	Medium	$2.11 \times 10^6$		$3.893 \times 10^{-3}$	2.56		
	Fine	$3.82 \times 10^6$		$3.852 \times 10^{-3}$	0.15		
Full-scale ship ( $Fr=0.26$ )	Coarse	$2.86 \times 10^6$	$2.33 \times 10^{-3}$	$2.112 \times 10^{-3}$	-9.36	0.45	4.36
	Medium	$4.59 \times 10^6$		$2.197 \times 10^{-3}$	-5.71		
	Fine	$8.55 \times 10^6$		$2.235 \times 10^{-3}$	-4.08		

**Table 3.** Time convergence study

	$\Delta t$ (s)	$C_T$ [42,36]	$C_T$ of CFD	Error (%)	$R_G$	$TCI$ (%)
Model-scale ship ( $Fr=0.108$ )	0.028	$3.796 \times 10^{-3}$	$3.998 \times 10^{-3}$	5.35	0.86	15.84
	0.02		$3.893 \times 10^{-3}$	2.56		
	0.014		$3.852 \times 10^{-3}$	0.16		
Full-scale ship ( $Fr=0.26$ )	0.07	$2.33 \times 10^{-3}$	$2.153 \times 10^{-3}$	-7.60	0.84	10.49
	0.05		$2.197 \times 10^{-3}$	-5.71		
	0.035		$2.234 \times 10^{-3}$	-4.12		

**Table 4** Convergence study for model-scale ( $Fr=0.108$ ,  $\eta/B=1.3$  and  $H/T=1.3$ )

Grid set or $\Delta t$ (s)	Grid volumes	$C_T$ of CFD	$R_G$	$GCI$ or $TCI$ (%)
Coarse	$1.18 \times 10^6$	$7.15 \times 10^{-3}$	0.23	0.59
Medium	$2.11 \times 10^6$	$7.28 \times 10^{-3}$		
Fine	$3.41 \times 10^6$	$7.31 \times 10^{-3}$		
0.028		$7.21 \times 10^{-3}$	0.57	1.85
0.02		$7.28 \times 10^{-3}$		
0.014		$7.32 \times 10^{-3}$		

Monotonic convergence was achieved for all the terms. The errors were within an acceptable range, and the convergence rates were all within the range (0–1). Considering the computational resources and accuracy, the remaining computations were performed with medium grid numbers and medium time steps.

### 2.3 Self-propulsion point selection

The body force method was used to calculate the self-propelling point of the ship. First, a *PI* controller was used to determine the propeller speed when the ship reaches the target speed and then the value of the speed is input into fixed computations. The numerical calculation shows that the error between propeller thrust and ship resistance is within 2 %, which conforms to the requirements of subsequent computations. The virtual disk used the full-scale KP505 propeller open-water characteristics provided by the SIMMAN conference [43]. The propeller open-water curve and the location of the virtual disk are shown in Fig. 3. In the figure,  $J$  represents the propeller advance coefficient,  $K_T$  is the thrust coefficient,  $K_Q$  is the torque coefficient, and  $\eta$  is the open water efficiency.

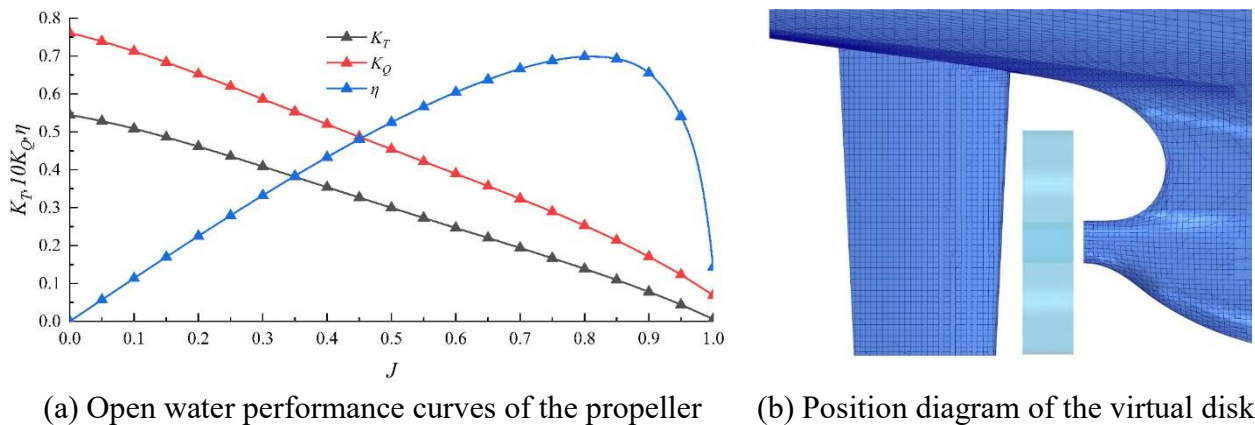


Fig. 3. Figure of the propeller

Fig. 4 displays the duration curves of the full-scale ship velocity  $U$  and propeller rotation speed  $n$  during the self-propulsion validation process, and Table 5 shows a comparison of the full-scale ship self-propulsion calculation results from this paper with those from other studies.

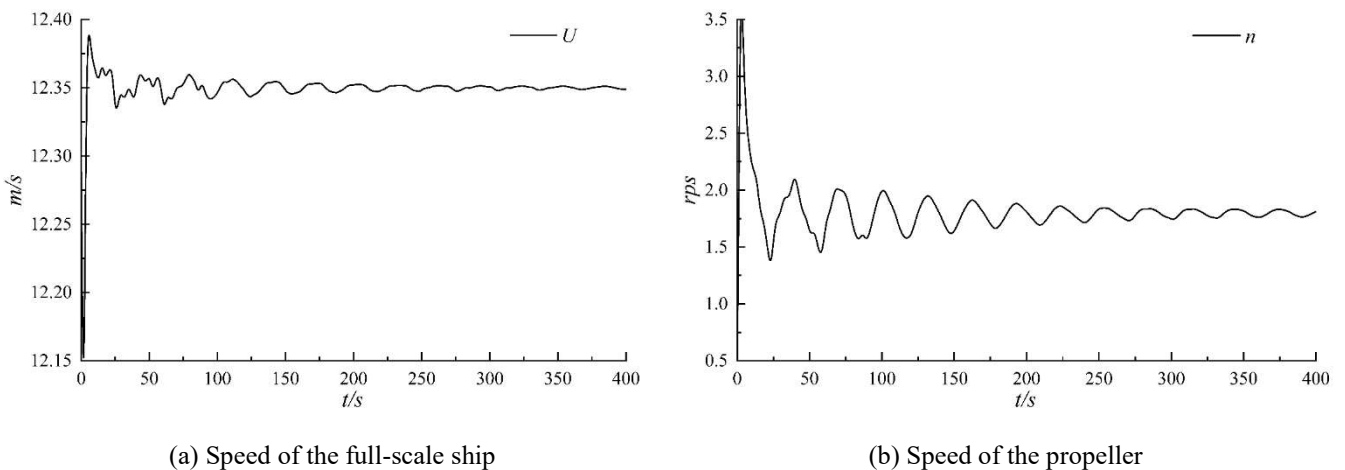


Fig. 4. Time duration curves of full-scale ship speed and propeller rotation speed

Based on these figures and tables, it is feasible to use a virtual disk to determine the self-propulsion point and the calculated results are within an acceptable range. Using this method, the propeller rotational speed of the full-scale ship is determined to be 0.71 rps when  $Fr=0.108$ .

**Table 5.** Grid calculation results of full-scale ship self-propulsion ( $Fr=0.26$ )

Parameters	Results of this article	Song et al. (w Rudder)[44]	Can et al. (w Rudder)[45]	Castro et al. (w/o Rudder)[36]
$C_T$	$2.687 \times 10^{-3}$	$2.583 \times 10^{-3}$	$2.772 \times 10^{-3}$	$2.773 \times 10^{-3}$
$n$ (rps)	1.787	1.737	1.719	1.736
Error of $C_T$ (%)	-	4.03	-3.07	3.10
Error of $n$ (%)	-	2.88	3.96	2.94

### 3. Numerical simulation results and analysis

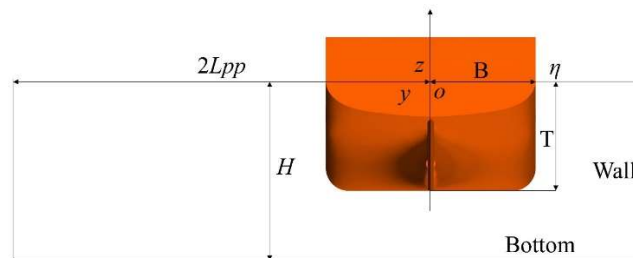
#### 3.1 Calculation of the calculation cases

In this study, the shallow water and bank effects of ships with scale effects were analysed using a fully fixed ship model. Ships typically navigate at slow speeds in restricted waters. Therefore,  $Fr=0.108$  was assumed in this study to calculate various water depths and ship-bank distances for both the ship model and full-scale ship (with or without a virtual disk). To take into account the influence of a single-sided bank on the ship, the right-sided bank was designated as the near-ship side. The calculation cases are listed in Table 6. Calculations for the scenarios  $\eta/B=1.3, 1.5, 2.0$  and  $H/T=1.3, 1.5, 2.0$ , were performed for model-scale ships and full-scale ships with and without propellers, resulting in a total of 27 numerical calculation cases. In addition, two more scenarios were added for full-scale ships without propeller and with propeller, namely  $H/T=1.3$ ,  $\eta/B=3.0$  and  $H/T=3.0$ ,  $\eta/B=1.3$ . Therefore, 31 numerical calculations were considered in this study.

Fig. 5 is a schematic representation of the computational domain, with  $H$  symbolising the water depth of the computational domain, and  $\eta$  denotes the horizontal distance from the longitudinal section of the ship to the bank. The virtual disk is abbreviated as VD, and the conditions with and without the propeller are denoted as w VD and w/o VD, respectively.

**Table 6.** Calculation cases ( $Fr=0.108$ )

Type	Scale ratio	w or w/o VD	$n$ (rps)	$\eta/B$	$H/T$
Model-scale	31.6	w/o	-	1.3, 1.5, 2.0, 3.0	1.3, 1.5, 2.0, 3.0
Full-scale	1	w/o	-		
Full-scale	1	w	0.71		

**Fig. 5.** Diagram of water depth and ship-bank distance

#### 3.2 Analysis of hull forces

To facilitate a comparison of the results, the calculation results were non-dimensionalised in this study. The formulae for the surge force coefficient  $C_T$ , pressure coefficient  $C_P$ , sway force coefficient  $C_Y$ , and yaw moment coefficient  $C_N$  are expressed as Equations (7)–(10) as follows:

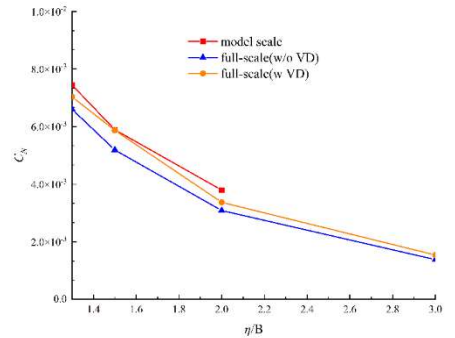
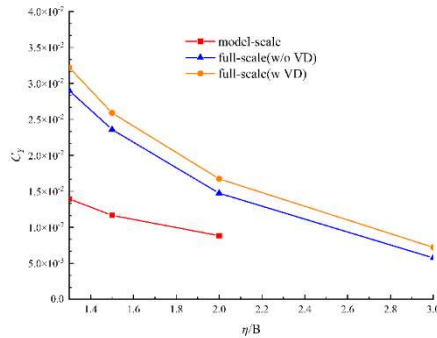
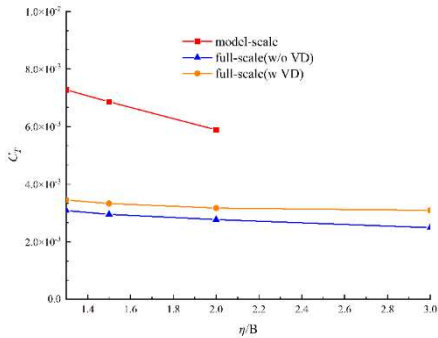
$$C_T = \frac{F_T}{0.5\rho U^2 S} \tag{7}$$

$$C_P = \frac{P - \rho gh}{0.5\rho U^2} \tag{8}$$

$$C_Y = \frac{F_Y}{0.5\rho U^2 L_{PP} T} \tag{9}$$

$$C_N = \frac{M_N}{0.5\rho U^2 L_{PP}^2 T} \tag{10}$$

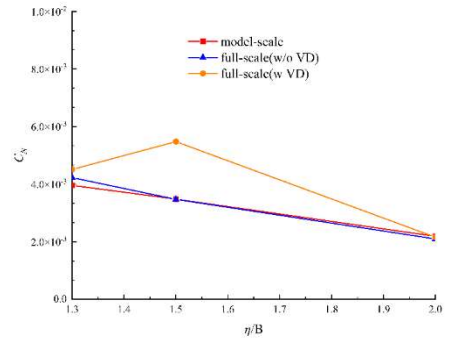
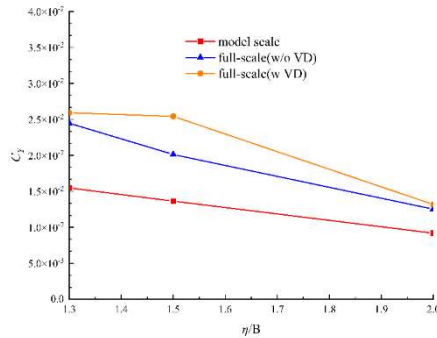
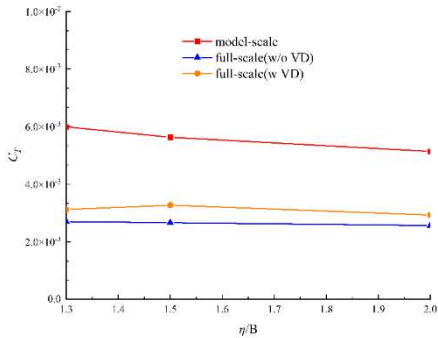
where  $F_T$  is the surge force of the ship,  $\rho$  is the density of the water,  $U$  is the set speed,  $S$  is the wet surface area of the ship,  $P$  is the total pressure,  $T$  is the draft of the ship,  $g$  is the acceleration due to gravity,  $H$  is the depth of the water,  $L_{PP}$  is the length of the ship's plumb line,  $F_Y$  is the ship's  $y$ -direction force, and  $M_N$  is yaw moment.



(a) Surge force coefficient,  $H/T=1.3$

(b) Sway force coefficient,  $H/T=1.3$

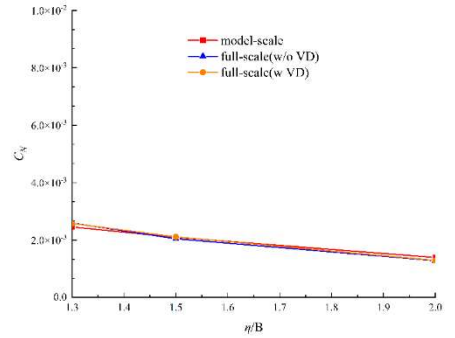
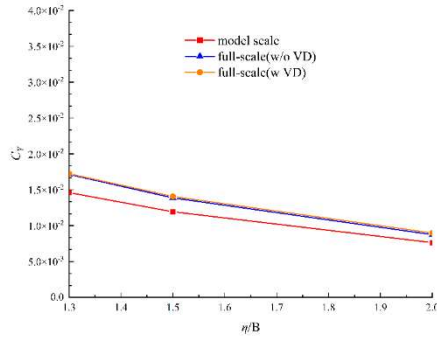
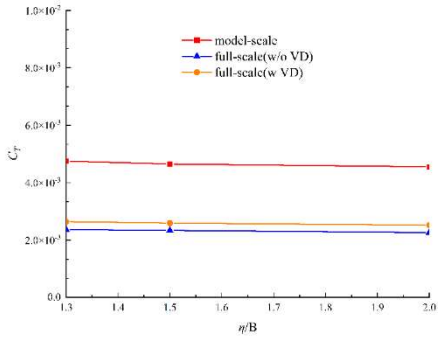
(c) Yaw moment coefficient,  $H/T=1.3$



(d) Surge force coefficient,  $H/T=1.5$

(e) Sway force coefficient,  $H/T=1.5$

(f) Yaw moment coefficient,  $H/T=1.5$



(g) Surge force coefficient,  $H/T=2.0$

(h) Sway force coefficient,  $H/T=2.0$

(i) Yaw moment coefficient,  $H/T=2.0$

**Fig. 6** Ship forces of different cases

When ships navigate in confined waters, the forces on their hull change because of bank and shallow water effects, generating surge, sway, and yawing forces that affect the manoeuvrability of the ship. When the Froude number is equal, the Reynolds number of the full-scale ship is higher. The water flow between the ship and bottom/ship and bank was compressed, leading to more pronounced displacement and enlargement effects, and consequently creating a more severe low-pressure zone in the midsection of the full-scale ship. Fig. 6 depicts the variations in the surge force, sway force, and yaw moment of the ships with the ship-bank distance when  $H/T$  is 1.3 to 2.0 times. To better observe the waveform under different scale ratios, the waveform was dimensionless in this study,  $Wave = Position\ z/L_{PP}$ , where  $Position\ z$  represents the height of the free water surface in the vertical direction, and  $L_{PP}$  represents the length of the ship. Fig. 7 shows the pressure fraction distribution and the waveform for a full-scale ship w VD when  $H/T=1.5$ . The waveforms of different cases at  $H/T=1.3$  is shown in Fig. 8.

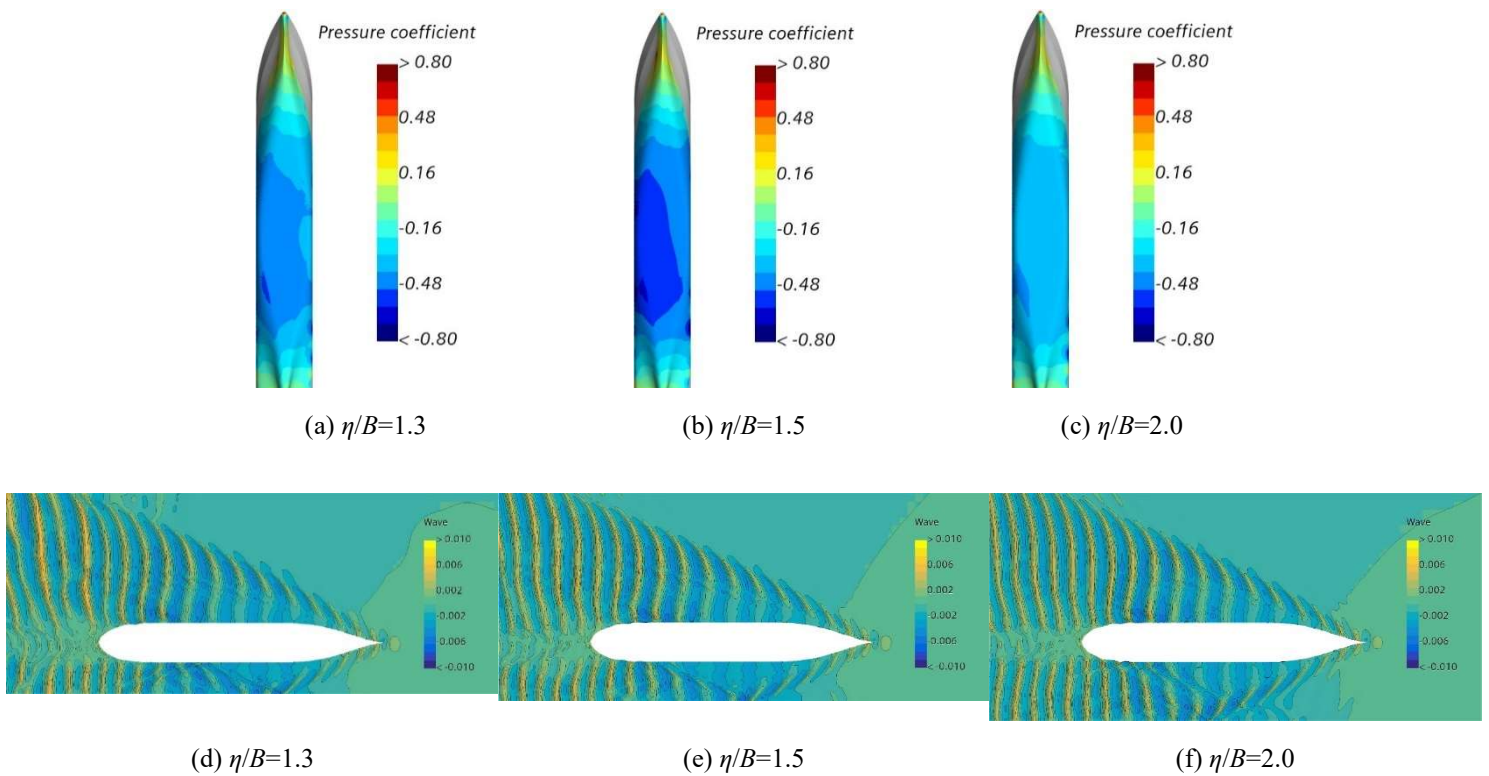


**Fig. 7.** Pressure fraction and waveform of full-scale (w VD) at  $H/T=1.5$

In extremely shallow water conditions  $H/T=1.3$ , the influence of the water current on the ship is greatest. Therefore, the parameters of ship-bank distance are increased to 3.0, to collect more data on flow field variations. The graph leads to the following conclusions:

(1) It is widely recognised that the variances between the resistance coefficients and the yaw moment coefficients of the model and full-scale ships originate from the influence of scale effects, as discussed by Zeng et al. [12]. In most of the cases, the variation trend of the associated coefficients of the model-scale ship is identical to that of the full-scale ship, implying that the force and yaw moment coefficients decrease with the increase of  $H/T$  and  $\eta/B$ . However, there are outliers, such as in extreme shallow water conditions ( $H/T=1.3$ , as shown in Fig. 6 (a) and (b), where the change in the surge force coefficient and sway force coefficient of the model-scale ship appears more pronounced than that of the full-scale ship, which is obviously due to the superimposed effects of scale and shallow water.

(2) In most of the calculation cases, regardless of water depth and bank distance, the trend in their impact on the ship's hydrodynamic characteristics is such that as the water depth or bank distance gradually increases, the coefficients of longitudinal resistance, sway force, and yaw moment of the hull decrease, with one exception for the full-scale ship w VD at  $H/T=1.5$  and  $\eta/B=1.5$ . There are several reasons for this anomalous

situation. One of them could be that the Kelvin waves generated by the ship hull create reflection waves when they encounter the wall, which then overlap with the newly generated Kelvin waves, as shown in Fig. 7 (e), increasing the wave strength and increasing the sway force and yaw moment coefficients. Figure 7 (a)–(c) clearly shows the surface pressure of the ship in this case. For example, Hoydonck et al. [24] provided evidence that under conditions with gradually increasing  $\eta/B$  at  $H/T=1.35$ , the sway force coefficient and the yaw moment coefficient of the propeller-equipped KVLCC2 do not simply decrease monotonically, but instead exhibit a sudden increase at  $\eta/B=0.76$ . Both the present study and [24] show that the effect of water on a ship in confined waters is far more complex than expected, which also agrees with Liu et al. and Degrieck [40,46]. The trends in force and moment might not change monotonically, but may show an oscillating curve, although the  $H/T$  and  $\eta/B$  values are different in the two papers and the types of ships used are also different.

(3) The corresponding parameters of full-scale ships w VD are greater than those of full-scale ships w/o VD. With an increase in the water depth to ship draft ratio ( $H/T$ ), the differences in the longitudinal resistance coefficient, sway force coefficient, and yaw moment coefficient between the w/o VD and w VD full-scale ships gradually decrease, excluding abnormal scenarios.

(4) At a water depth to ship draft ratio ( $H/T$ ) of 2.0, the sway force coefficient and yaw moment coefficient of full-scale ships, both w VD and w/o VD, are almost equivalent. However, the fact that the longitudinal resistance coefficient of the full-scale ship w VD remains greater than that of the ship w/o VD further demonstrates that the propeller's suction effect on accelerating the longitudinal flow persists.

Figure 9 illustrates that at a  $\eta/B$  ratio of 1.3, the longitudinal resistance coefficient, sway force coefficient, and yaw moment coefficient for scale-model ships w/o VD and full-scale ships w VD vary with changes in the water depth to ship draft ratio ( $H/T$ ).

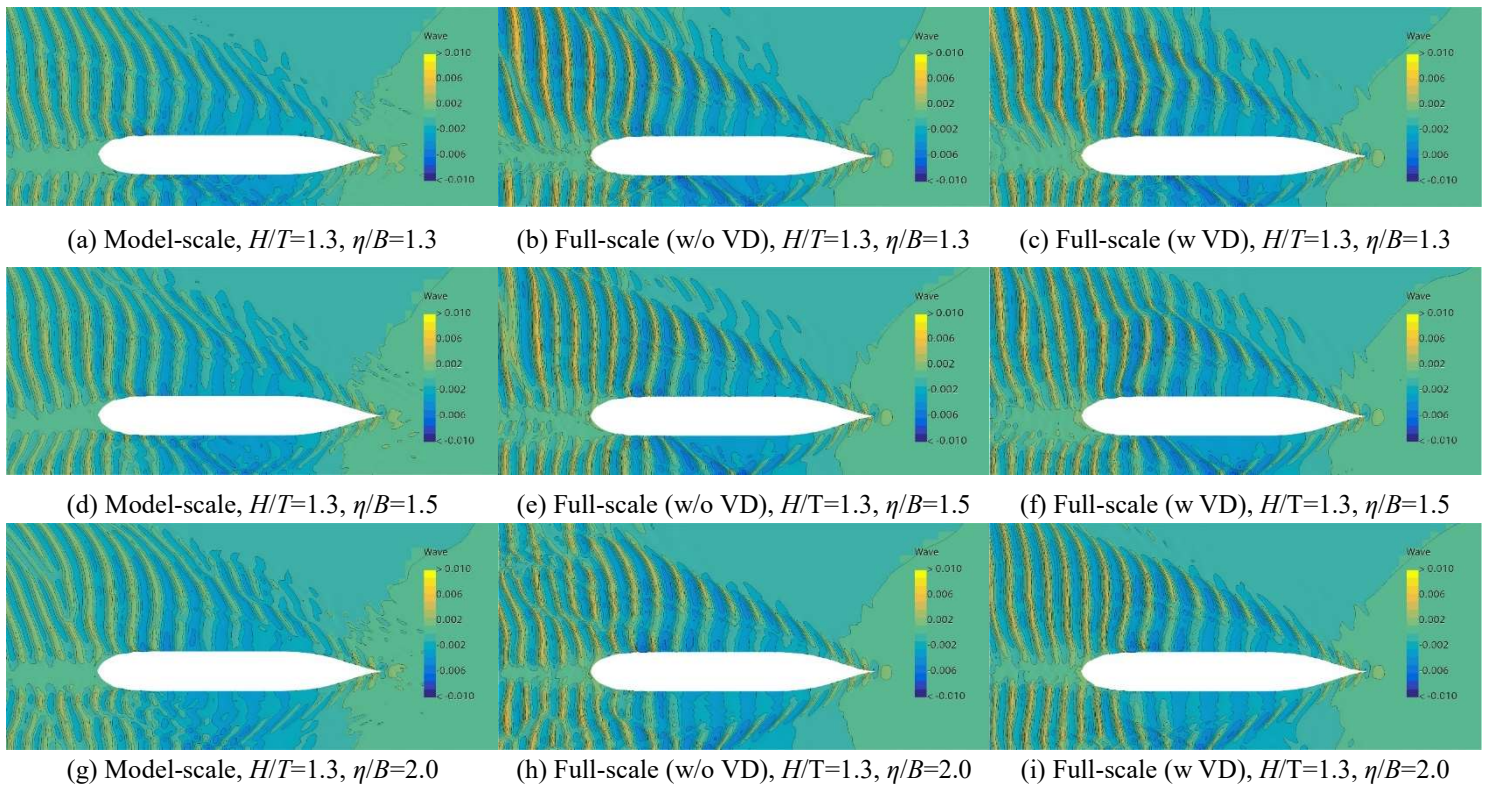


**Fig. 8.** Waveform of different cases

It can be seen from the figures that (1) as the ratio of  $H/T$  progressively increases, the longitudinal resistance coefficient, sway force coefficient, and yaw moment coefficient successively decrease; (2) when the ratio of  $H/T$  is greater than 2.0, the sway force coefficient and yaw moment coefficient of both full-scale ships w and w/o VD are essentially similar. This implies that when examining bank effects when the ship is situated in deeper waters, it is feasible to use full-scale ships w/o VD to explore the asymmetric sway forces

on the hull, thereby drastically reducing computational resource consumption and improving the calculation efficiency. Of course, this does not mean that a full-scale ship w/o VD can be used to analyse the changes in a ship's surge forces.

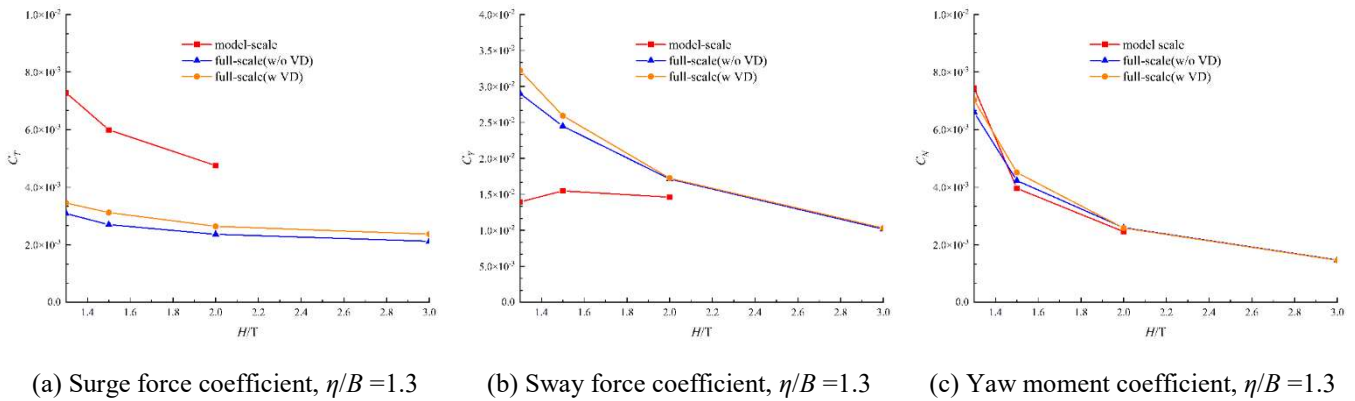


Fig. 9. Ship forces

### 3.3 Pressure and flow lines

Fig. 10 and Fig. 11 show the streamline flow direction and pressure fraction distribution for the model-scale ship, full-scale ship w/o VD, and full-scale ship w VD at  $\eta/B=1.3$  and  $H/T=1.3$ , the left side is starboard. The streamline illustrates the motion of fluid particles traversing the ship's surface, helping to analyse the force conditions on the hull.

(1) The streamlines on the starboard side of the hull (the side closer to the bank) were straight and concentrated, indicating a greater longitudinal flow velocity within this region. This led to a reduction in water pressure and the formation of a low-pressure area, as shown in the figure by the dark blue segment at the bottom of the ship. After passing the bow shoulder and the bilge section, the streamlines on the port side begin to deviate towards the starboard side.

(2) Owing to the effects of the stagnation point at the bow, the streamlines at the port side and at the bottom of the ship were deflected towards the port side in the front portion of the ship, moving away from the bank.

(3) At the model scale, the sway deviation of the ship surface streamlines is greater than that of the full-scale ship w/o VD and w VD, and a more pronounced streamline rotation is observed on the side near the bank at the stern of the model-scale ship. Around the stern, the flow is separated and reversed owing to the bottom and bank constraints. Hoydonck et al. pointed out that water converges at the bilge, indicating a strong bilge vortex [24]. The restriction of the flow causes the flow to separate, and reversal occurs [35].

(4) The pressure distributions across the surfaces of the three ships varied, where in the low-pressure area at the bottom of the full-scale ship w VD has a larger proportion to the wetted surface area of the hull. A larger low-pressure area at the bottom of the full-scale ship w VD leads to greater sway displacement. Using a model-scale ship to study the sway displacement of the hull led to conservative results.

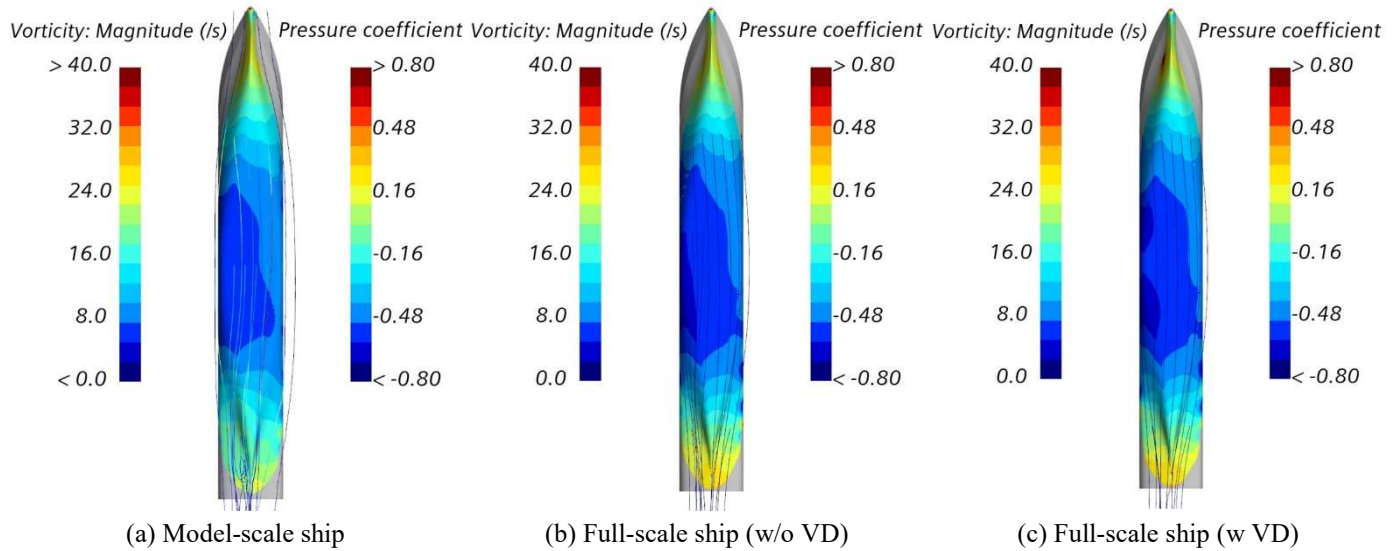


**Fig. 10.** Schematic diagram of hull surface pressure and flow lines

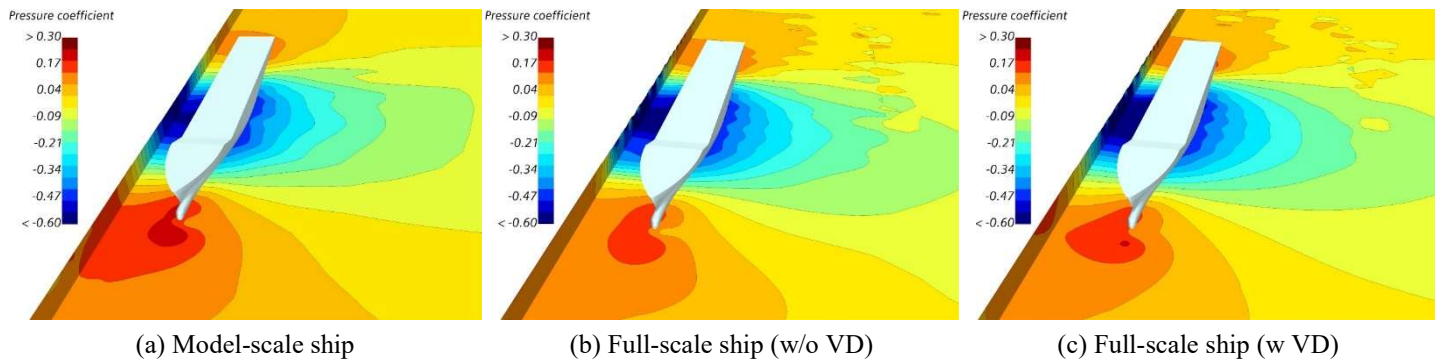


**Fig. 11.** Schematic diagram of the bottom and wall

### 3.4 Streamline distribution of the stern surface

Fig. 12 depicts the distribution of flow lines at the stern of the model-scale ship and the full-scale ship w/o VD and w VD under the conditions of different  $\eta/B$  and  $H/T$  (on the side of the starboard).

As can be observed from the figures:

(1) There are several areas of backflow at the stern of the model-scale ship, as denoted by positions A, B, and C, and outlined by dashed lines in Fig. 12 (a). The backflow area in region A was aligned with that illustrated in Fig. 10 (a), indicating that they were the same backflow area. The backflow in region B is associated with the shape of the stern and results from the flow-line deviation when water flows down over the tail fin and past the stern post. Region C signifies that the rudder is also within the stern backflow area of the ship. By analysing the flow direction of the flow lines, it can be inferred that regions B and C possibly belong to the same backflow area.

(2) The flow lines in regions A and C at the stern of the full-scale ship without a propeller become straight and stream towards the rear of the ship. For the full-scale ship w VD, the flow lines in regions A and C also straighten, and the flow line deviation in region B nearly disappeared.

(3) The flow direction at the stern of the ship changed as the  $H/T$  increased in the calculation cases. Figs. 12 (d), (e), and (f) show the results. The occurrence of water flow streamlines bending to form recirculation areas in Regions B and C was limited to model-scale ships. Straight streamlines flowing towards the rear of the ship were present at the stern of both w/o VD and w VD full-scale ships. This demonstrates that with a gradual increase in  $H/T$  in the calculation cases, the asymmetry in the ship's flow pattern brought about by the unilateral wall will decrease, which means that the asymmetry will be less evident.

(4) The asymmetry of the ship's flow pattern also decreases when  $\eta/B$  is increased in the calculation cases. This is shown in Figs. 12 (g), (h), and (i). However, it is evident that increasing  $\eta/B$  causes only a minor reduction in asymmetry, an effect that is less significant than increasing  $H/T$ .

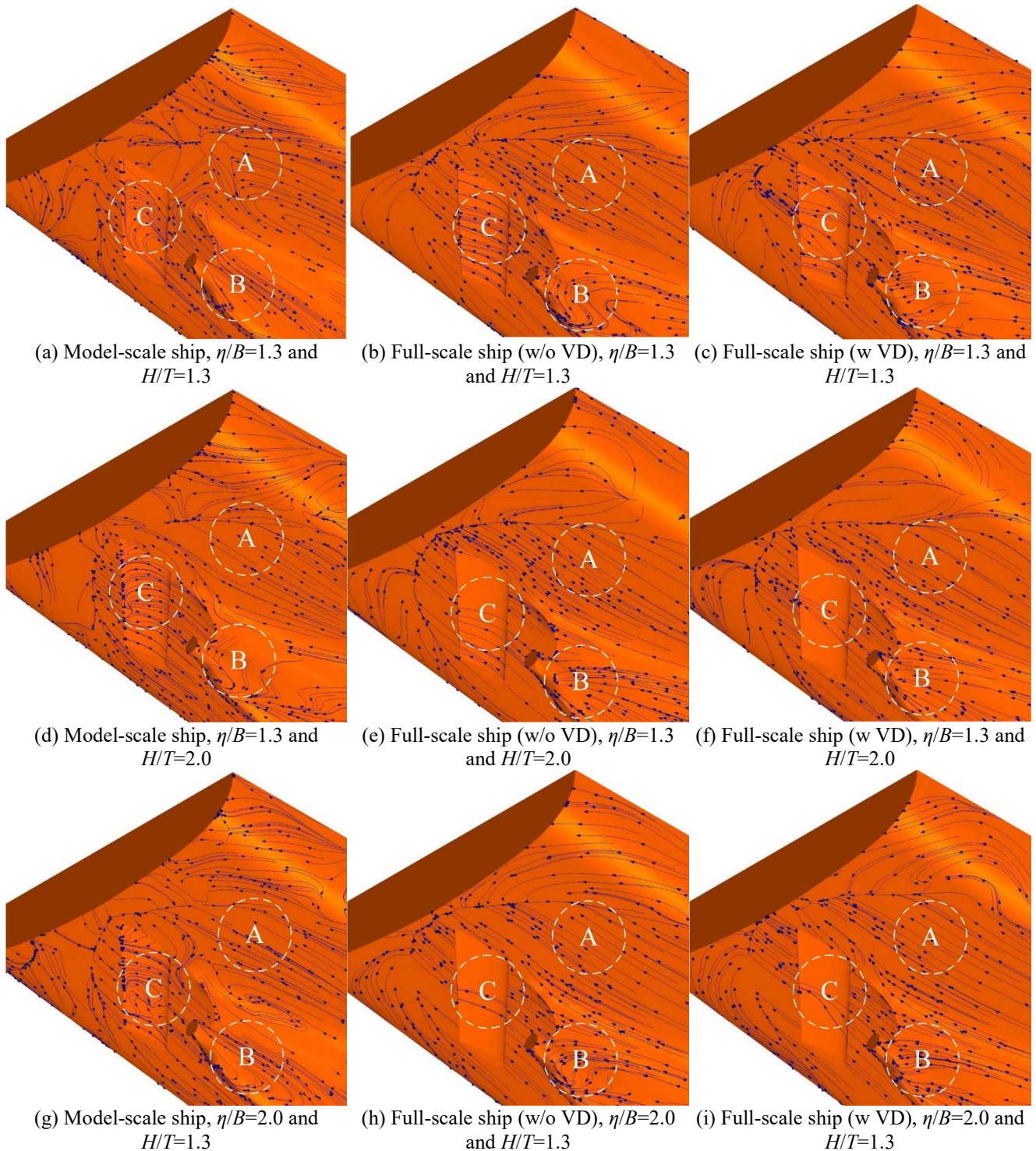


**Fig. 12.** Distribution of streamlines

### 3.5 Wake fraction at the stern

When the ship navigates close to the bank, the wake fraction at the stern deviates towards the bank side. A large high wake fraction emerged at the model scale, whereas the wake fraction at the stern was much

smaller at the full scale than at the model scale. The wake fraction at the ship's stern for the conditions of different  $\eta/B$  and  $H/T$  are depicted in Fig. 13.

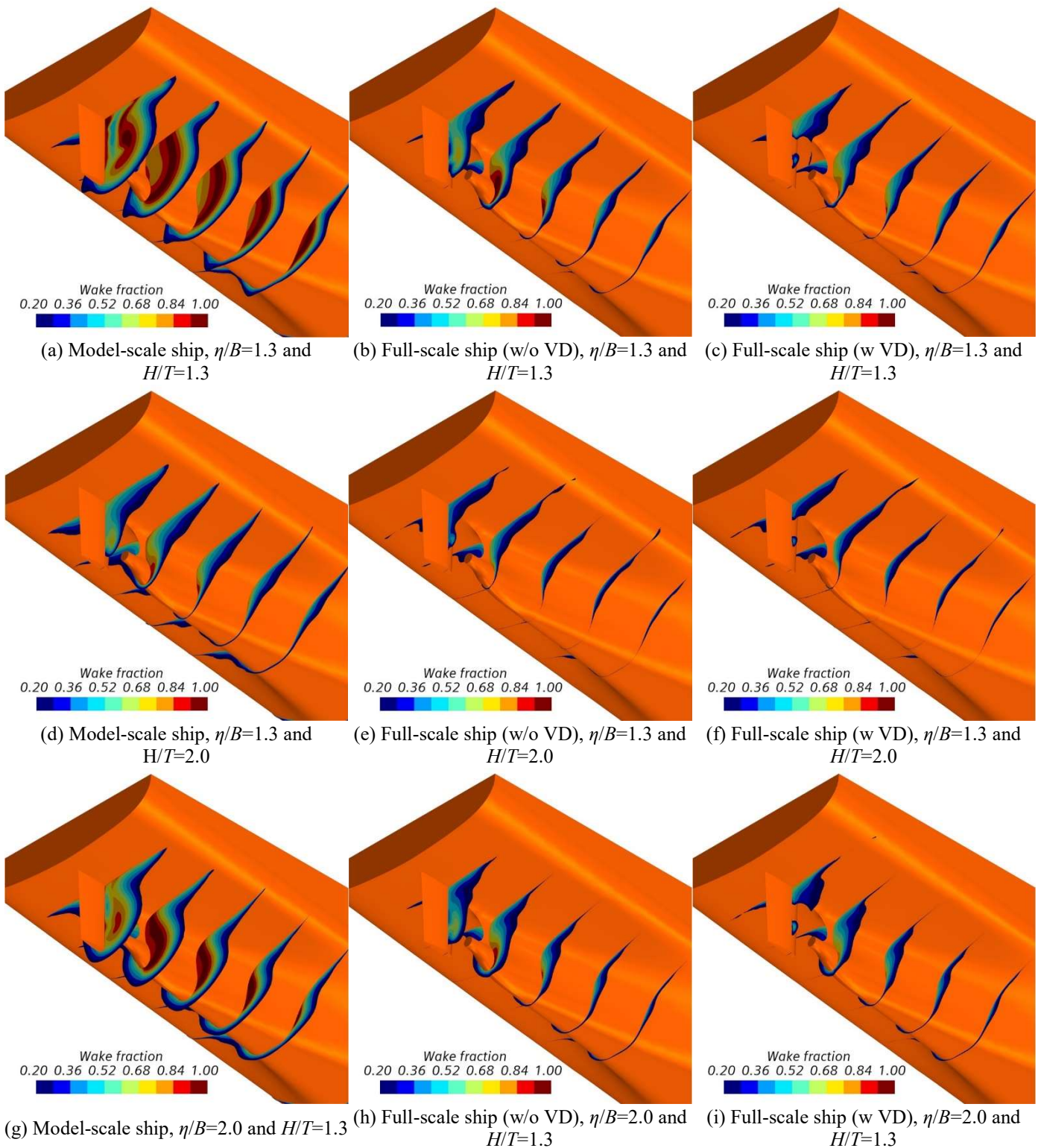


Fig. 13. Wake fraction at the stern

Fig. 13 illustrates the distribution of wake flow at the ship's stern for the computational scenarios with  $\eta/B=1.3$  and  $H/T=1.3$ . It can be seen from the figure that:

(1) As the ship approached the bank, the wake fraction distribution at the stern underwent a transition from a symmetrical state in the absence of the bank wall to an asymmetrical position with respect to the bank side.

(2) The stern of the model-scale ship has a large area with a high-wake region, whereas the stern of the full-scale ship has a significantly smaller area with a high-wake region. This indicated that the flow velocity at the stern of the model-scale ship was lower than at the stern of the full-scale ship. This is expected to cause the model-scale ship’s stern propeller to operate in a flow field environment with a lower advance coefficient, causing the thrust and torque coefficients of the model-scale ship’s stern propeller to be greater than those of the full-scale ship. The wake characteristics are improved when the computational model is changed from model-scale ship to full-scale ship. This allows the propeller to operate more efficiently as it receives a fast and homogeneous inflow.

(3) The area of the wake fraction at the stern of the full-scale ship w VD is less than that at the stern of the full-scale ship w/o VD, which is primarily attributed to the accelerating effect of the propeller on the flow velocity at the stern. In addition, the suction action of the propeller has slightly reduced the asymmetry in the distribution of the wake region.

(4) The asymmetry of the wake fraction at the ship’s stern is reduced when the  $H/T$  and  $\eta/B$  are increased in the calculated calculation cases. However, similar to the analysis in Fig. 12 above, the effect of reducing the asymmetry by increasing  $\eta/B$  is lower than that of increasing  $H/T$ .

### 3.5.1 Migration characteristics of wake fraction at propeller disk

Near the bank, the ship’s stern exhibited an uneven flow speed distribution, with a hook-shaped area of high wake fraction at the propeller disk shifting towards the bank and the bottom. Under full-scale conditions, the effects of the bank wall and water depth on the wake fraction at the propeller disk were less pronounced than those at the model-scale, with the high wake fraction region being substantially smaller and the hook-shaped wake less pronounced. This effect also diminishes with the varying distance from the bank.

We set the distance between the ship and bank and the draft-to-depth ratio to observe their effects on the wake deviation. Fig. 14 and 15 show  $\eta/B=1.3$  and  $H/T=1.3$ , and the changes in the average wake fraction at the propeller disk. The average wake fractions at the propeller disk surface of the model-scale ship and full-scale ship without VD are listed in Tables 7 and 8.

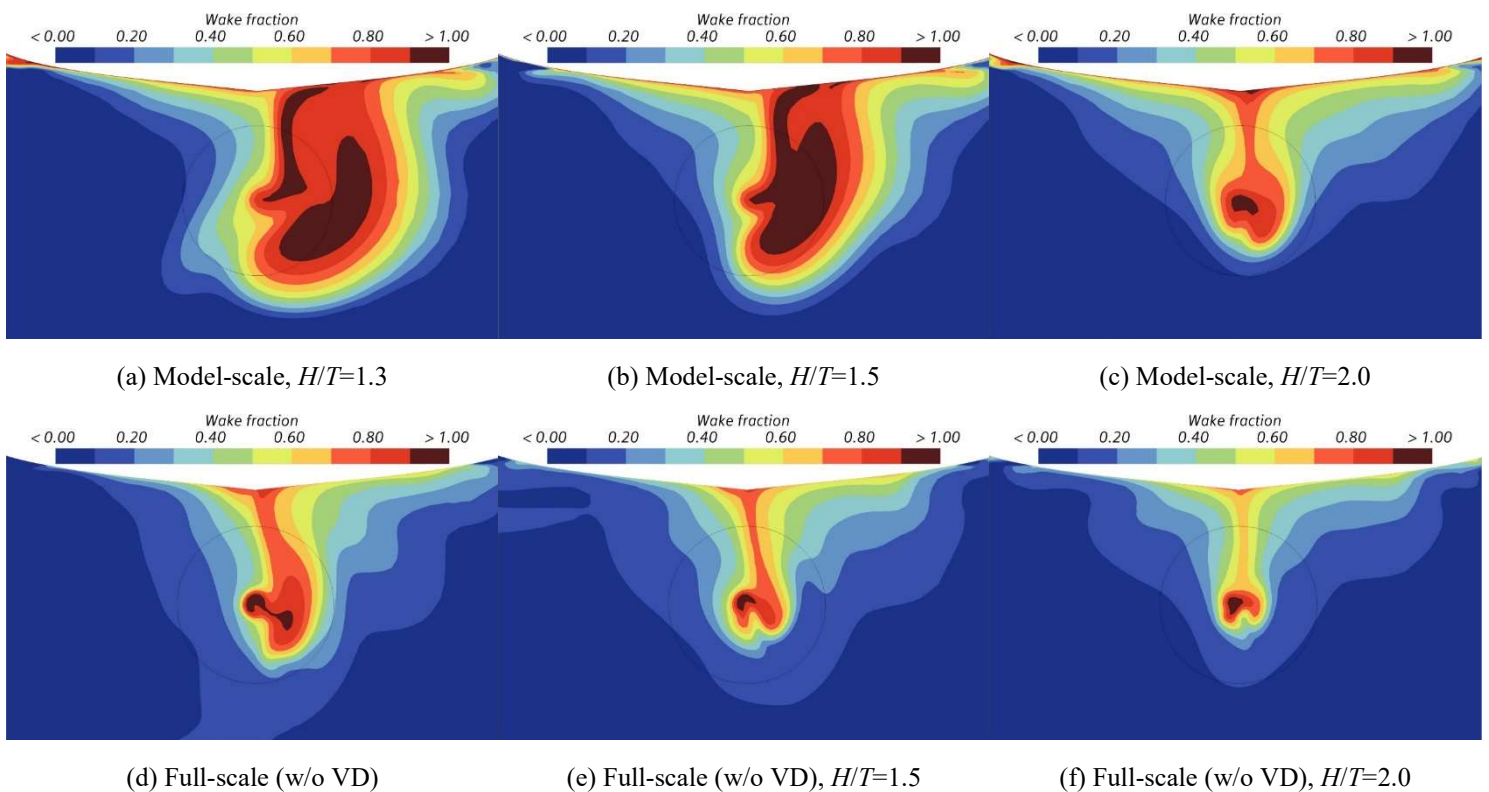


**Fig. 14** When  $\eta/B=1.3$ , the wake fraction at the propeller disk with water depth

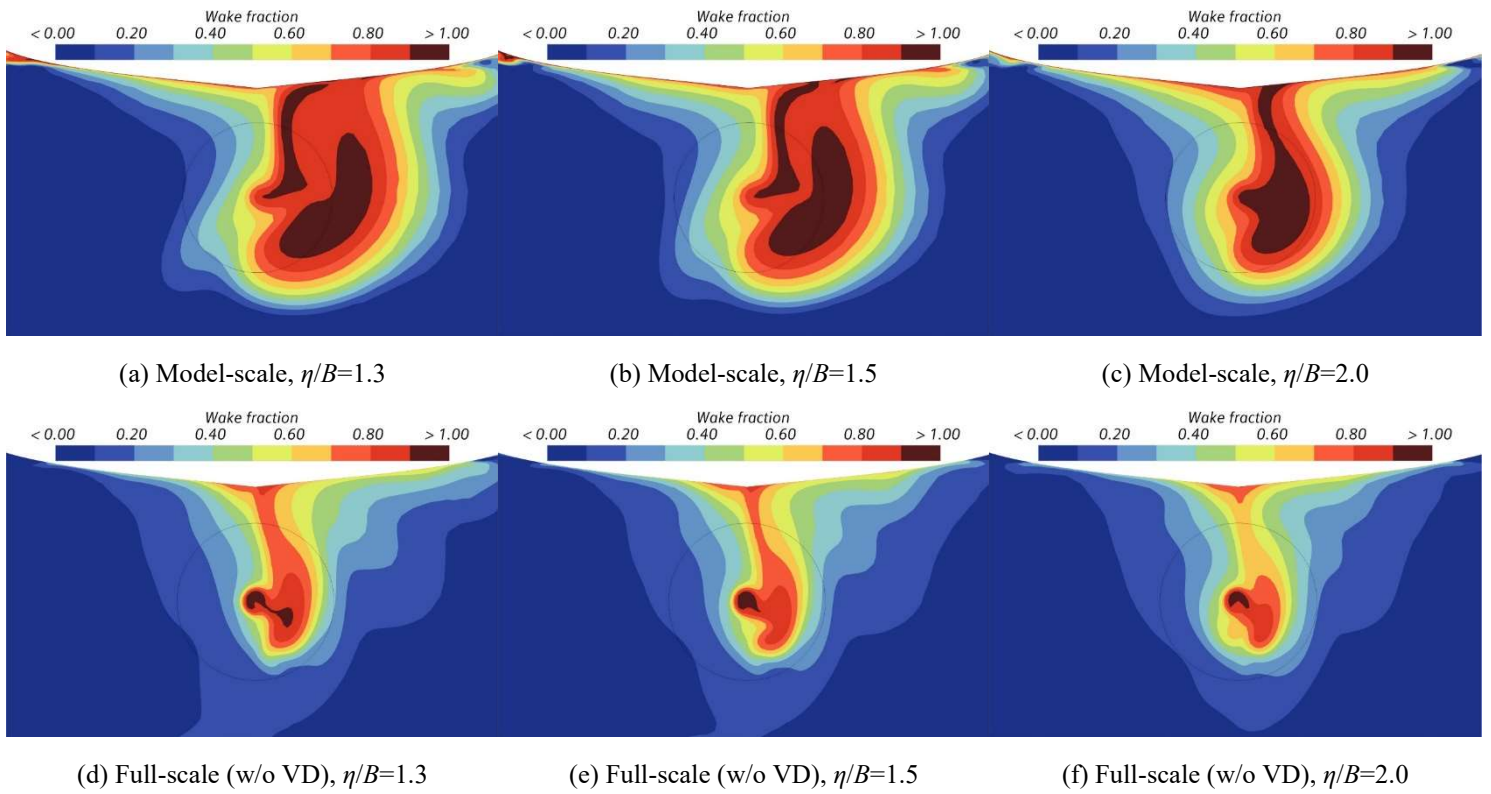


**Fig. 15.** When  $H/T=1.3$ , the wake fraction at the propeller disk with distance from the bank.

The positive direction of the y-axis was defined as  $0^\circ$ , looking clockwise from the stern to the bow in a positive direction. The circumferential distribution of the wake fraction with the water depth at  $r/R=0.5$ , and  $r/R=1.0$  at  $\eta/B=1.3$  is shown in Fig. 16(a) and b. The circumferential distribution of the wake fraction with the bank distance at  $r/R=0.5$ , and  $r/R=1.0$  at  $H/T=1.3$  is shown in Fig. 16(c), (d). Here,  $r$  is the radius of the propeller disk surface and  $R$  is the propeller radius.

**Table 7.** Average wake fraction at the ship propeller disk surface (model-scale)

$\omega_X$	$H/T=1.3$	$H/T=1.5$	$H/T=2.0$
$\eta/B=1.3$	0.610	0.579	0.466
$\eta/B=1.5$	0.615	0.594	0.466
$\eta/B=2.0$	0.653	0.594	0.459

**Table 8** Average wake fraction at the ship propeller disk surface (full-scale w/o VD)

$\omega_X$	$H/T=1.3$	$H/T=1.5$	$H/T=2.0$
$\eta/B=1.3$	0.428	0.335	0.257
$\eta/B=1.5$	0.422	0.332	0.255
$\eta/B=2.0$	0.418	0.337	0.258

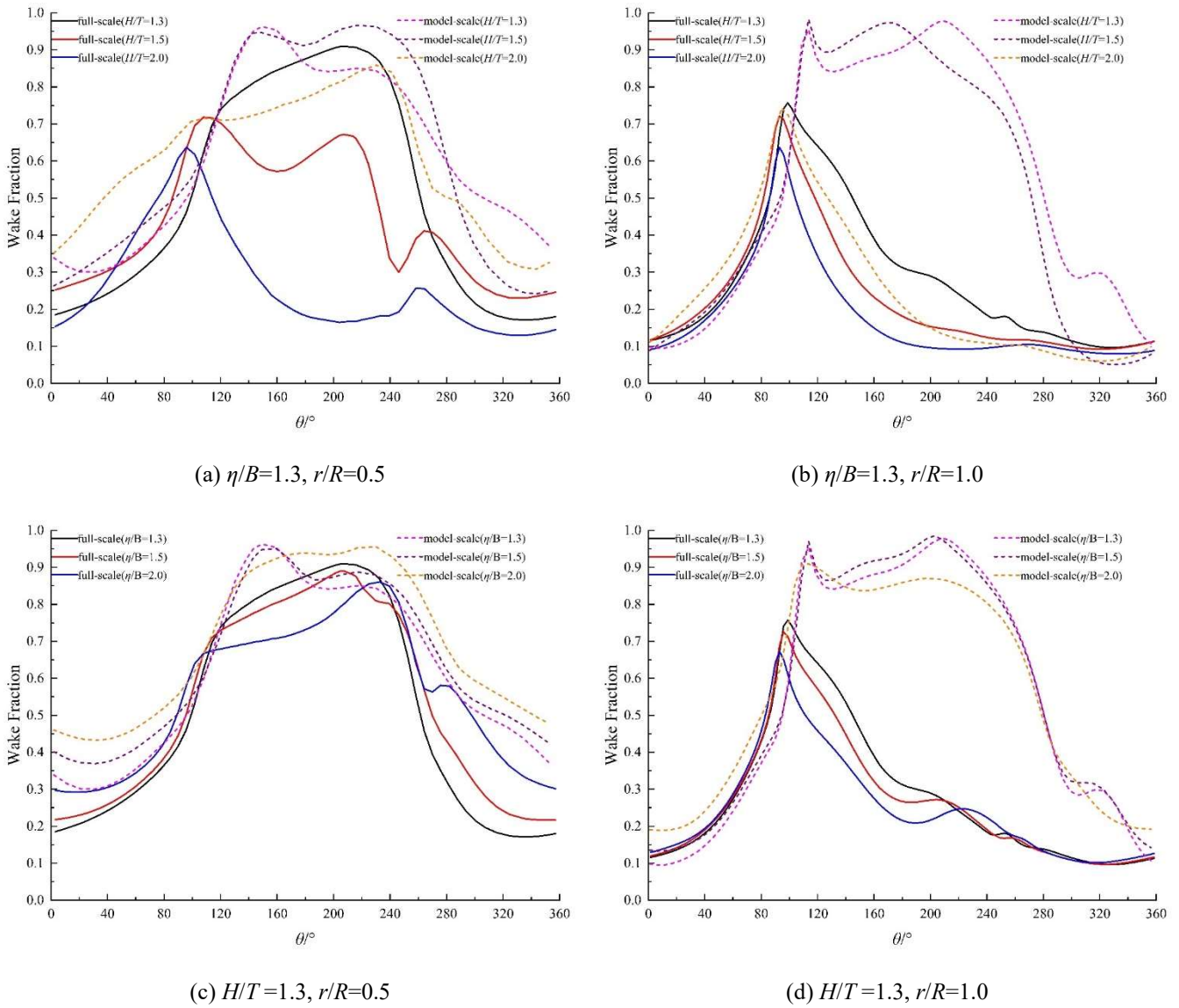


**Fig. 16.** Circumferential distribution of the wake fraction at the propeller disk

The average wake fraction progressively decreased with increasing  $H/T$ . The average wake fraction for the ship model was more strongly influenced by the water depth and bank distance than that of the full-scale ship. As the ship-to-bank distance increases, the high-wake fraction area at the propeller disk is continuously corrected and reduced.

### 3.5.2 Effect of the propeller

We selected the positions 0.1 m before the virtual disk surface to investigate and analyse the wake in confined waters caused by the suction effect of the propeller, which is simulated by the virtual disk using the body-force method. Fig. 17 and 18 show the schematic diagram of the wake fraction and the circumferential distribution of the wake fraction at the selected positions when  $\eta/B=1.3$  and  $H/T=1.3$ . They show the wake fraction at the plane located 0.1 m ahead of the virtual disk for full-scale ships w/o VD and w VD. Tables 9 and 10 show the wake fraction at the plane of 0.1 m on the front surface of the virtual disk of full-scale ships w/o VD and w VD.

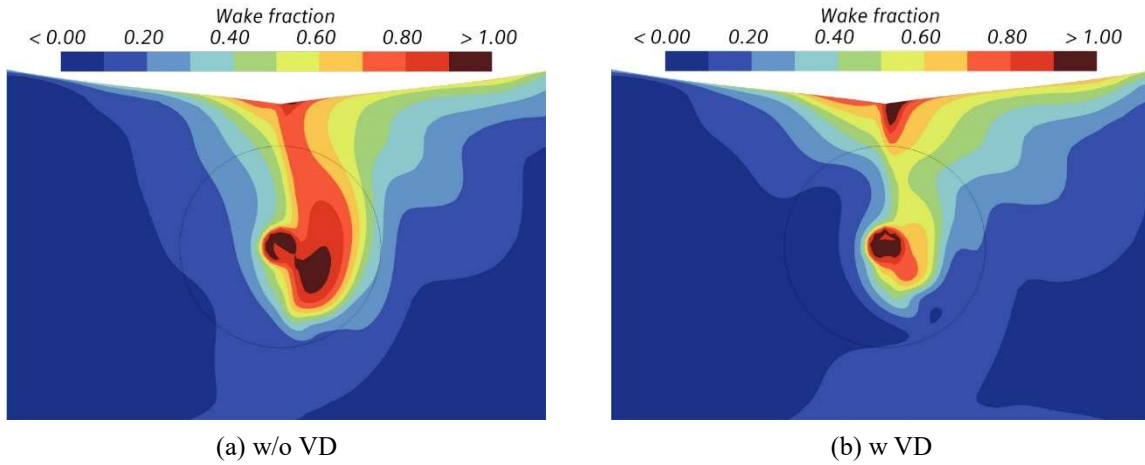


Fig. 17. Wake fraction distribution

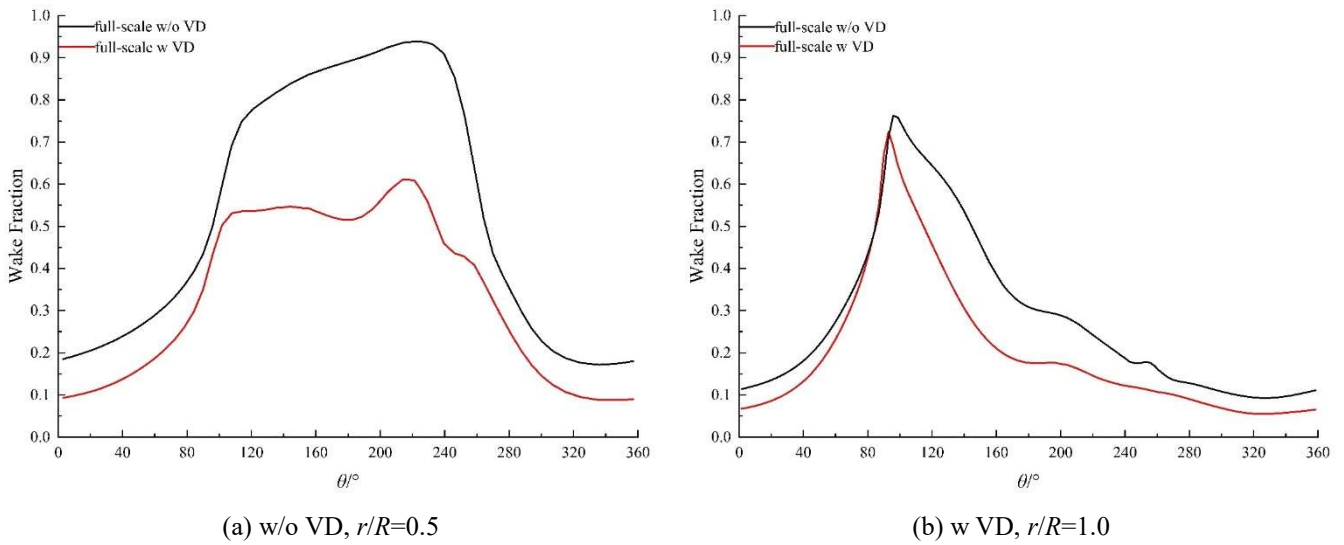


Fig. 18. Circumferential distribution of the wake fraction ( $H/T=1.3, \eta/B=1.3$ )

Table 9. Average wake fraction (w/o VD)

$\omega_X$	$H/T=1.3$	$H/T=1.5$	$H/T=2.0$
$\eta/B=1.3$	0.444	0.346	0.262
$\eta/B=1.5$	0.433	0.338	0.260
$\eta/B=2.0$	0.426	0.343	0.262

Table 10. Average wake fraction (w VD)

$\omega_X$	$H/T=1.3$	$H/T=1.5$	$H/T=2.0$
$\eta/B=1.3$	0.269	0.232	0.180
$\eta/B=1.5$	0.277	0.273	0.184
$\eta/B=2.0$	0.279	0.237	0.183

Because of the streamlining effect of the propeller, the wake fraction was more concentrated at the stern in the calculations for the propeller-equipped ship, and the propeller created a suction effect on the longitudinal water flow, increasing the inflow at the propeller disk. While navigating in confined waters, the wake contracts

towards the propeller hub, reducing the wake at the stern of the ship. This, in turn, partially mitigates the effects of the shallow water and the wall.

#### 4. Conclusions

This study focuses on the international standard container ship KCS, and numerical hydrodynamic computations were performed on three types of ships—model-scale ships, full-scale ships without propellers, and full-scale ships with propellers under varying water depth to draft ratios and ship-bank distance conditions. The forces acting on the hull, the pressure distribution on the hull surface, and the wake fraction at the stern were computed. The influences of the scale effect and the propeller flow field were studied. The conclusions are as follows.

(1) As is generally known, the differences between the force and moment coefficients of the model-scale ship and the full-scale ship stem from the scale effects. However, under extremely shallow water conditions, the changes in the longitudinal drag and sway force coefficients of the model-scale ship were more drastic than those of the full-scale ship. This is probably due to the combined influence of scale and shallow-water effects.

(2) The effects of the water depth and distance to the bank on the hydrodynamics of the three types of ships showed in most situations that the ship's longitudinal drag coefficient, sway force coefficient, and yaw moment coefficient progressively decreased with increasing water depth or bank distance. However, scenarios with inconsistent change trends indicate that the effects of water on ships in restricted waters are far more complex than expected. The fluctuations in the forces and moments' variation trend may not follow a monotonic pattern, but instead display oscillatory characteristics.

(3) In most cases, the relevant parameters of the full-scale ship w VD exceed those of the full-scale ship w/o VD. As the water depth to draft ratio  $H/T$  increases, the differences in the longitudinal drag coefficient, sway force coefficient, and yaw moment coefficient between the full-scale ship w/o VD and the full-scale ship w VD gradually decrease. However, even under conditions of substantial water depth to draft ratio, the longitudinal drag coefficient of the full-scale ship w VD remains higher, indicating the persistent influence of the propeller suction on the accelerating longitudinal water flow.

(4) Under the condition of the model-scale, the cross-flow deflection of the streamlines on the ship's hull surface is greater than that of full-scale ships w/o VD and w VD, with a more noticeable rotation of the streamlines appearing on the side of the model-scale ship's stern that is in closer proximity to the bank. The cross-flow deflection of the streamlines on a full-scale ship w VD surface is minimal, and one of the contributing factors is probably the suction effect of the propeller.

(5) The stern of the model-scale ship featured a substantially high wake fraction, whereas the high wake fraction of the full-scale ship stern was significantly smaller.

(6) The wake fraction at the stern of a full-scale ship w VD is less than that at the stern of a full-scale ship w/o VD. In addition, the suction effect of the propeller reduces the wake fraction asymmetry to a certain degree.

#### REFERENCES

- [1] Zou, L., Larsson, L., 2013. Confined water effects on the viscous flow around a tanker with propeller and rudder. *International Shipbuilding Progress*, 60(1-4), 309-343.
- [2] Lee, S. M., Lee, B. K., 2019. Study on the squat characteristics of very large tanker and container ship in shallow water. *29<sup>th</sup> International Ocean and Polar Engineering Conference (ISOPE 2019)*, June 16–21, Honolulu, USA.
- [3] Terziev, M., Tezdogan, T., Incecik, A. 2022. Scale effects and full-scale ship hydrodynamics: A review. *Ocean Engineering*, 245, 110496. <https://doi.org/10.1016/j.oceaneng.2021.110496>
- [4] Shivachev, M., Khorasanchi, M., Day, A. H., 2017. Trim Influence on Kriso Container Ship (KCS): An Experimental and Numerical Study. *36<sup>th</sup> International Conference on Ocean, Offshore and Arctic Engineering*, June 25-30, Trondheim, Norway. <https://doi.org/10.1115/OMAE2017-61860>
- [5] Simonsen, C. D., Otzen, J. F., Joncquez, S., Stern, F., 2013. EFD and CFD for KCS heaving and pitching in regular head waves. *Journal Of Marine Science and Technology*, 18(4), 435-459. <https://doi.org/10.1007/s00773-013-0219-0>

- [6] Shevchuk, I., Böttner, C. U., Kornev, N., 2019. Numerical investigation of scale effects on squat in shallow water. *5<sup>th</sup> International Conference on Ship Manoeuvring in Shallow and Confined Water*, 19-23 May, Ostend, Belgium.
- [7] Song, K., Guo, C., Wang, C., Sun, C., Li, P., Zhong, R., 2020. Experimental and numerical study on the scale effect of stern flap on ship resistance and flow field. *Ships and Offshore Structures*, 15(9), 981-997. <https://doi.org/10.1080/17445302.2019.1697091>
- [8] Duffy, J., 2008. Modelling of Ship-Bank Interaction and Ship Squat for Ship-Handling Simulation. Ph.D. thesis, *University of Tasmania*, Tasmania, Australia.
- [9] Kok, Z., Duffy, J., Chai, S., Jin, Y., Javanmardi, M., 2020. Numerical investigation of scale effect in self-propelled container ship squat. *Applied Ocean Research*, 99, 102143. <https://doi.org/10.1016/j.apor.2020.102143>
- [10] Terziev, M., Terzogan, T., Incecik, A., 2021. A numerical assessment of the scale effects of a ship advancing through restricted waters. *Ocean Engineering*, 229, 108972. <https://doi.org/10.1016/j.oceaneng.2021.108972>
- [11] Shevchuk, I., Böttner, C. U., Kornev, N., 2016. Numerical analysis of the flow in the gap between the ship hull and the fairway bottom in extremely shallow water. *4<sup>th</sup> International Conference on Ship Manoeuvring in Shallow and Confined Water with Special Focus on Ship Bottom Interaction*, 23-25 May, Hamburg, Germany.
- [12] Zeng, Q., Hekkenberg, R., Thill, C., Hopman H., 2020. Scale effects on the wave-making resistance of ships sailing in shallow water. *Ocean Engineering*, 212, 107654. <https://doi.org/10.1016/j.oceaneng.2020.107654>
- [13] Li, T., Sun, S., 2023. Numerical study on the scale effects of two-dimensional cycloidal propellers. *Ocean Engineering*, 279, 114445. <https://doi.org/10.1016/j.oceaneng.2023.114445>
- [14] Mikulec, M., Piehl, H., 2023. Verification and validation of CFD simulations with full-scale ship speed/power trial data. *Brodogradnja*, 74 (1), 41-62. <https://doi.org/10.21278/brod74103>
- [15] Demirel, Y. K., Turan, O., Incecik, A., 2017. Predicting the effect of biofouling on ship resistance using CFD. *Applied Ocean Research*, 62, 100-118. <https://doi.org/10.1016/j.apor.2016.12.003>
- [16] Farkas, A., Degiuli, N., Martić, I., 2018. Assessment of hydrodynamic characteristics of a full-scale ship at different draughts. *Ocean Engineering*, 156, 135-152. <https://doi.org/10.1016/j.oceaneng.2018.03.002>
- [17] Song, S., Demirel, Y. K., Atlar, M., 2019. An investigation into the effect of biofouling on the ship hydrodynamic characteristics using CFD. *Ocean Engineering*, 175, 122-137. <https://doi.org/10.1016/j.oceaneng.2019.01.056>
- [18] Niklas, K., Pruszko, H., 2019. Full scale CFD seakeeping simulations for case study ship redesigned from V-shaped bulbous bow to X-bow hull form. *Applied Ocean Research*, 89, 188-201. <https://doi.org/10.1016/j.apor.2019.05.011>
- [19] Mikkelsen, H., Walther, J. H., 2020. Effect of roughness in full-scale validation of a CFD model of self-propelled ships. *Applied Ocean Research*, 99, 102162. <https://doi.org/10.1016/j.apor.2020.102162>
- [20] Zhang, Y. X., Chen, K., Jiang, D. P., 2020. CFD analysis of the lateral loads of a propeller in oblique flow. *Ocean Engineering*, 202, 107153. <https://doi.org/10.1016/j.oceaneng.2020.107153>
- [21] Dogrul, A., 2022. Numerical Prediction of Scale Effects on the Propulsion Performance of Joubert BB2 Submarine. *Brodogradnja*, 73(2), 17-42. <https://doi.org/10.21278/brod73202>
- [22] Đurasević, S., Gatin, I., Uroić, T., Jasak, H., 2022. Partially rotating grid method for self-propulsion calculations with a double body ship model. *Ocean Engineering*, 266, 113105. <https://doi.org/10.1016/j.oceaneng.2022.113105>
- [23] Liu, H., Ma, N., Gu, X. C., 2018. Experimental Study on Ship-Bank Interaction of Very Large Crude Carrier in Shallow Water. *Journal of Shanghai Jiao Tong University*, 23(6), 730-739. <https://doi.org/10.1007/s12204-018-1999-5>
- [24] Hoydonck, W. V., Toxopeus, S., Eloot, K., Bhawsinka, K., Queutey, P., Visonneau, M., 2019. Bank effects for KVLCC2. *Journal Of Marine Science and Technology*, 24(1), 174-199. <https://doi.org/10.1007/s00773-018-0545-3>
- [25] Hadi, E. S., Tuswan, T., Ghina, A., Baharuddin, A., Samuel, S., Muhammad, L. H., Muhammad R. C. P. H., Muhammad, I., Dian, P. S., Dendy, S., 2023. Influence of the canal width and depth on the resistance of 750 DWT Perintis ship using CFD simulation. *Brodogradnja*, 74, (1), 117-144. <https://doi.org/10.21278/brod74107>
- [26] Yuan, Z. M., 2019. Ship Hydrodynamics in Confined Waterways. *Journal of Ship Research*, 63(1), 16-29. <https://doi.org/10.5957/JOSR.04170020>
- [27] Elsherbiny, K., Tezdogan, T., Kotb, M., Incecik, A., Day, S., 2019. Experimental analysis of the squat of ships advancing through the New Suez Canal-ScienceDirect. *Ocean Engineering*, 178, 331-344. <https://doi.org/10.1016/j.oceaneng.2019.02.078>
- [28] Raven, H. C., 2019. Shallow-water effects in ship model testing and at full scale. *Ocean Engineering*, 189, 106343. <https://doi.org/10.1016/j.oceaneng.2019.106343>
- [29] Ulgen, K., Dhanak M. R., 2022. Hydrodynamic Performance of a Catamaran in Shallow Waters. *Journal of Marine Science and Engineering*, 10, 1169. <https://doi.org/10.3390/jmse10091169>
- [30] Lee, S., 2023. Hydrodynamic interaction forces on different ship types under various operating conditions in restricted waters. *Ocean Engineering*, 267, 113325. <https://doi.org/10.1016/j.oceaneng.2022.113325>

- [31] Poojari, D. B., Kar, A. R., 2016. Effect of lateral and depth restriction on ship behavior using computational fluid dynamics. *4<sup>th</sup> International Conference on Ship Manoeuvring in Shallow and Confined Water with Special Focus on Ship Bottom Interaction*, 23-25 May, Hamburg, Germany.
- [32] Lo, D. C., Lin, I. F., 2009. Applying computational fluid dynamics to simulate bank effects. *19<sup>th</sup> International Offshore and Polar Engineering Conference*, 21-26 June, Osaka, Japan.
- [33] Zou, L., Larsson, L., Delefortrie, G., Lataire, E., 2011. CFD prediction and validation of ship-bank interaction in a canal. *2<sup>nd</sup> International conference on Ship Manoeuvring in Shallow and Confined Water: Ship to ship interaction*, 18 - 20 May, Trondheim, Norway.
- [34] Zou, L., 2012. CFD predictions including verification and validation of hydrodynamic forces and moments on ships in restricted waters. Ph.D. thesis, *Chalmers University of Technology*, Gothenburg, Sweden.
- [35] Zou, L., Larsson, L., 2013. Confined water effects on the viscous flow around a tanker with propeller and rudder. *International Shipbuilding Progress*, 60(1-4), 309-343.
- [36] Castro, A. M., Carrica, P. M., Stern, F. L., 2011. Full scale self-propulsion computations using discretized propeller for the KRISO container ship KCS. *Computers & Fluids*, 51(1), 35-47. <https://doi.org/10.1016/j.compfluid.2011.07.005>
- [37] Carrica, P. M., Mofidi, A., Eloit, K., Delefortrie, G., 2016. Direct simulation and experimental study of zigzag maneuver of KCS in shallow water. *Ocean Engineering*, 112, 117-133. <https://doi.org/10.1016/j.oceaneng.2015.12.008>
- [38] Islam, H., Soares C. G., 2022. Estimation of hydrodynamic derivatives of an appended KCS model in open and restricted waters. *Ocean Engineering*, 266, 112947. <https://doi.org/10.1016/j.oceaneng.2022.112947>
- [39] Menter, F. R., 1994. Two-equation eddy-viscosity turbulence models for engineering applications. *AIAA Journal*, 32(8), 1598-1605. <https://doi.org/10.2514/3.12149>
- [40] Liu, H., Ma, N., Gu, X., 2021. CFD prediction of ship-bank interaction for KCS under extreme conditions. *Journal of Marine Science and Technology*, 26, 1062-1077. <https://doi.org/10.1007/s00773-021-00798-x>
- [41] Lee, S., Hong, C., 2017. Study on the course stability of very large vessels in shallow water using CFD. *Ocean Engineering*, 145, 395-405. <https://doi.org/10.1016/j.oceaneng.2017.09.064>
- [42] Tokyo 2015: A Workshop on CFD in Ship Hydrodynamics KRISO Container Ship (KCS), 2015. [https://t2015.nmri.go.jp/Instructions\\_KCS/Case\\_2.1/Case\\_2-1.html](https://t2015.nmri.go.jp/Instructions_KCS/Case_2.1/Case_2-1.html). accessed 20<sup>th</sup> July 2023.
- [43] SIMMAN (2020). Workshop on Verification and Validation of Ship Manoeuvring Simulation Methods, 2020. <https://simman2020.kr/contents/KCS.php>. accessed 20<sup>th</sup> July 2023.
- [44] Song, S., Demirel, Y. K., Atlar, M., 2020. Penalty of hull and propeller fouling on ship self-propulsion performance. *Applied Ocean Research*, 94, 102006. <https://doi.org/10.1016/j.apor.2019.102006>
- [45] Can, U., Delen, C., Bal, S., 2020. Effective wake estimation of KCS hull at full-scale by GEOSIM method based on CFD. *Ocean Engineering*, 218, 108052. <https://doi.org/10.1016/j.oceaneng.2020.108052>
- [46] Degrieck, A., 2017. Ship-bank interaction: comparison between experimental and numerical results. MSc thesis, *University of Lisbon*, Lisbon, Portugal.